CHEMISTRY OF MATERIALS

ARTICLE

pubs.acs.org/cm

First-Order Phase Transition in a New $CaCu_5$-Related Antimonide, $CePt_5Sb$

L. Salamakha,[†,‡] E. Bauer,[*,†] H. Michor,[†] G. Hilscher,[†] H. Müller,[†] R. Svagera,[†] O. Sologub,[§,⊥] P. Rogl,[§] J. Hester,[||] T. Roisnel,[#] G. Giester,[△] and S. Mudryi[‡]

[†]Institute of Solid State Physics and [△]Institute of Mineralogy and Crystallography, Vienna University of Technology, A-1040 Wien, Austria

[§]Institute of Physical Chemistry, University of Vienna, A-1090 Wien, Austria

[‡]Department of Physics of Metals, Lviv National University, 79005 Lviv, Ukraine

[||]Bragg Institute, ANSTO, Locked Bag 2001, Kirrawee DC, NSW, 2232, Australia

[#]Centre de Diffractométrie X, Sciences Chimiques de Rennes, UMR 6226 CNRS - Université de Rennes 1, 35042 Rennes, France

Supporting Information

ABSTRACT: A new $CaCu_5$ related antimonide, $CePt_5Sb$, has been identified. This ternary compound undergoes a structural phase transition at about 80 K according to room- and low-temperature X-ray and neutron diffraction, and measurements of electrical resistivity, specific heat and magnetism. The room temperature phase forms a new rhombohedral structure, space group $R\bar{3}$, a = 0.53535(2) nm, c = 3.10814(12) nm and consists of alternating blocks of $CaCu_5$- and $MnCu_2Al$-type fragments that extend along the c-axis. The low-temperature phase is monoclinic, space group Cm, a = 0.91821(5) nm, b = 0.53696(1) nm, c = 1.08064(6) nm, β = 107.40(1)°. The unit cells of both structures (orthohexagonal and monoclinic) are geometrically related via the transformation matrix $a' = -b'$, $b' = -a$, $c' = {}^1/_3b - {}^1/_3c$. Bulk properties elucidate the phase transition being of first-order and evidence Kondo interactions at low temperatures.

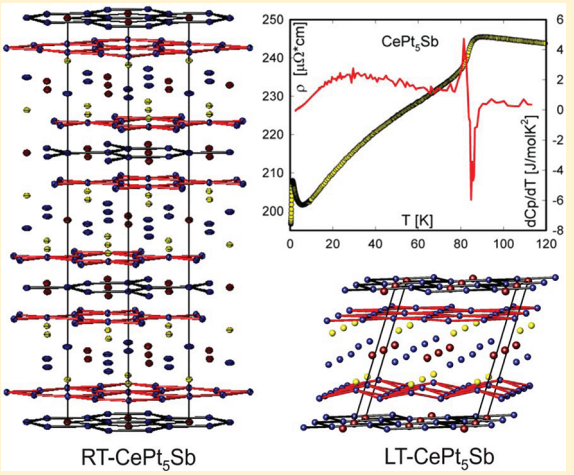

KEYWORDS: cerium platinum antimonide, $CePt_5Sb$, X-ray single-crystal diffraction, powder neutron diffraction, structure analysis, low-temperature first-order phase transition, electrical resistivity, specific heat, magnetism

INTRODUCTION

Ternary rare earth antimonides attract much attention because of their notable transport and magnetic properties and remarkable structures.[1−4] Among them, two groups of compounds, the so-called complex antimonides, i.e., filled skutterudites and $Yb_{14}MnSb_{11}$, are continuously under investigation because of their promising thermoelectric properties;[5−7] the former one is intensively studied by our research group.[8] As to ternary rare earth antimonides with higher content of transition metal, they also show a rich variety of interesting physical phenomena. Large Seebeck coefficient (~110 μV/K at 300 K) has been reported for $Ce_3Pt_3Sb_4$;[9,10] Kondo behavior and intermediate valence state were observed for CeRhSb[11] and CeIrSb,[12] respectively. More recently, a considerable progress has been delivered by the study of transport and magnetic properties of Heusler- and half Heusler-phases $REPd_2Sb$ ($MnCu_2Al$-type, RE = Y, Gd−Er) and REPdSb (MgAgAs-type, RE = Y, Dy−Er).[13] Although the equiatomic compounds showed half-metallic conductivity due to the formation of narrow gaps in their electronic band structures near the Fermi energy and exceptionally high Seebeck coefficient at room temperature, the compounds with larger transition metal content (1:2:1 phases) in contrast were found to be semimetals and their thermoelectric power is much lower. All compounds revealed complex character of their electronic structure with multiple electron and hole bands with different temperature and magnetic field variations of carrier concentrations and their mobilities.

Relatively less studies have been done for the RE-T-Sb systems (RE-rare earth metal, T-transition metal) with T content >50 at.%. In our effort to find new compounds with spectacular structure and distinctive properties, we came recently across the Ce−Pt−Sb system. Except layered $BaAl_4$-type derivative $CePt_{2+x}Sb_{2-y}$,[14] a new compound $CePt_5Sb$ was observed for which we established a new structural arrangement composed of $CaCu_5$- and $MnCu_2Al$-type fragments. In general, the unit cell of $CaCu_5$ serves as a structural building block for the formation of a variety ternary structures among borides, silicides, aluminides, gallides, germanides and stannides.[15−17] The compounds of $CaCu_5$-type and its

Received: June 5, 2011
Revised: July 19, 2011
Published: August 05, 2011

Table 1. Crystal Structure Data for RT- $CePt_5Sb$ (new structure type, space group $R\bar{3}$ (No. 148), single-crystal X-ray diffraction, Nonius KappaCCD, MoK_α) and LT-$CePt_5Sb$ (new structure type, space group Cm (No. 8), powder neutron diffraction, $\lambda = 1.622$ Å)[a]

nominal composition	$Ce_{14.3}Pt_{71.4}Sb_{14.3}$	$Ce_{14.3}Pt_{71.4}Sb_{14.3}$
formula from refinement	$CePt_5Sb$	$CePt_5Sb$
range for data collection	$3.94 < 2\theta < 69.88$	$1.55 < 2\theta < 160.00$
cryst size	$42 \times 42 \times 55\ \mu m^3$	
a (nm)	0.53535(2)	0.91821(5)
b (nm)		0.53696(1)
c [nm]	3.10814(12)	1.08064(6)
β (deg)		107.397(4)
T (K)	293	4.2
reflns in refinement	$650 F_o > 4\sigma(F_o)$ of 768	557
mosaicity	<0.5	
no. of variables	24	70
reliability factors	$R_F^2 = \Sigma\|F_0^2 - F_c^2\|/\Sigma F_0^2 = 0.0242$	$R_F = \Sigma\|F_o - F_c\|/\Sigma F_o = 0.093$; $R_I = \Sigma\|I_o - I_c\|/\Sigma I_o = 0.057$
R_{Int}	GOF= 1.061	$R_{exp} = [(N - P + C)/\Sigma w_i y^2_{oi})]^{1/2} = 0.044$; $\chi^2 = (R_{wP}/R_e)^2 = 5.2$
extinction (Zachariasen)	0.00014(2)	
M1; occupancy; U_{11}[b] = U_{22}; U_{33}; U_{12}; $U_{13} = U_{23} = 0$; B_{iso}[c]	3*b* (0,0,1/2); 1.00Ce1; 0.0152(3); 0.0104(5); 0.0075(2)	2*a* (*x*,0,*z*) *x* = 0.047(4); *z* = 0.746(3); 1.00Ce1; 0.6(4)
M2; occupancy; $U_{11} = U_{22}$; U_{33}; U_{12}; $U_{13} = U_{23} = 0$; B_{iso}	3*a* (0,0,0); 1.00Ce2; 0.0152(3); 0.0104(5); 0.0076(2)	2*a* (*x*,0,*z*) *x* = 0.526(3); *z* = 0.261(3); 1.00Ce2; 0.2(3)
M3; occupancy; U_{11}; U_{22}; U_{33}; U_{12}; U_{13}; U_{33}; B_{iso}	18*f* (*x*,*y*,*z*) *x* = 0.21559(7), *y* = 0.33485(6), *z* = 0.25999(1); 1.00Pt1; 0.0109(1); 0.0089(1); 0.0117(2); 0.00005(9); 0.0007(1); 0.0045(1)	4*b* (*x*,*y*,*z*) *x* = 0.238(2); *y* = 0.254(1); *z* = 0.051(2); 1.00Pt1; 0.2(2)
M4; occupancy; $U_{11} = U_{22}$; U_{33}; U_{12}; $U_{13} = U_{23} = 0$; B_{iso}	6*c* (0,0,*z*) *z* = 0.18665(2); 1.00Pt2; 0.0234(2); 0.0079(2); 0.01169(9)	4*b* (*x*,*y*,*z*) *x* = 0.404(2); *y* = 0.196(2); *z* = 0.476(2); 1.00Pt2; 0.4(2)
M5; occupancy; $U_{11} = U_{22}$; U_{33}; U_{12}; $U_{13} = U_{23} = 0$; B_{iso}	6*c* (0,0,*z*) *z* = 0.33402(2); 1.00Pt3; 0.0154(2); 0.0083(2); 0.00771(8)	2*a* (*x*,0,*z*)[d] *x* = 0.0; *z* = 0.0; 1.00Pt3; 0.9(5)
M6; occupancy; $U_{11} = U_{22}$; U_{33}; U_{12}; $U_{13} = U_{23} = 0$; B_{iso}	6*c* (0,0,*z*) *z* = 0.10556(3); 1.00Sb1; 0.0117(2); 0.0081(4); 0.0058(1)	2*a* (*x*,0,*z*) *x* = 0.129(2); *z* = 0.476(2); 1.00Pt4; 0.3(2)
M7; occupancy; B_{iso}		2*a* (*x*,0,*z*) *x* = 0.710(2); *z* = 0.813(2); 1.00Pt5; 0.8(4)
M8; occupancy; B_{iso}		2*a* (*x*,0,*z*) *x* = 0.371(3); *z* = 0.700(2); 1.00Pt6; 0.8(3)
M9; occupancy; B_{iso}		2*a* (*x*,0,*z*) *x* = 0.201(3); *z* = 0.253(3); 1.00Pt7; 0.9(4)
M10; occupancy; B_{iso}		2*a* (*x*,0,*z*) *x* = 0.891(3); *z* = 0.265(2); 1.00Pt8; 0.4(3)
M11; occupancy; B_{iso}		2*a* (*x*,0,*z*) *x* = 0.439(3); *z* = 0.958(3); 1.00Sb1; 0.5(4)
M12; occupancy; B_{iso}		2*a* (*x*,0,*z*) *x* = 0.663(3); *z* = 0.584(3); 1.00Sb2; 0.8(5)
residual e^- density; max; min in $(e^-/nm^3) \times 1000$	3.53; −2.95	

[a] Crystal structure data are standardized using the program Structure Tidy.[25] [b] Anisotropic atomic displacement parameters U_{ij} in 10^2 nm^2; [c] Isotropic atomic displacement parameters B_{iso} in 10^2 nm^2. [d] Fixed coordinate

derivatives are of much interest because, besides their practical application (e.g., rare earth-based AB_5-type alloys are extensively adopted for the negative electrode active material of Ni/MH rechargeable batteries,[18] $SmCo_5$ is the first-generation rare earth-transition metal-based permanent magnet[19]) they often show unexpected features such as superconductivity and intermediate valence state (e.g., $CeOs_3B_2$, $CeRu_3B_2$[16]), heavy fermion behavior (UCu_5Sn[17]), etc. As to antimonides, to the best of our knowledge, no ternary compounds with $CaCu_5$-type related structure have been ever reported. In this work, we describe the structure of a title compound, $CePt_5Sb$, both in its room-temperature (RT) and low-temperature (LT) forms determined by combination of X-ray and neutron diffraction and report on its transport properties and magnetism.

EXPERIMENTAL SECTION

Synthesis. A sample with the nominal composition $CePt_5Sb$ was prepared by argon arc-melting elemental pieces of Ce (Alfa Aesar, purity >99.9 mass%), Pt foil (Ögussa, Vienna, Austria) and Sb (ChemPur, Karlsruhe, Germany, 99.99 mass%). To ensure homogeneity, the sample was remelted several times and heat-treated in an evacuated silica tube for 14 days at 750 °C prior to quench by submerging the capsules in cold water.

Structural Characterization. For room-temperature X-ray single-crystal diffraction measurements, a crystal was mechanically isolated from the crushed alloy. Inspection on an AXS-GADDS texture goniometer assured high crystal quality, unit cell dimensions and Laue symmetry of the specimen prior to X-ray intensity data collection on a four-circle Nonius Kappa diffractometer equipped with a CCD area detector employing graphite monochromated Mo K_α radiation (λ = 0.071069 nm). Orientation matrix and unit-cell parameters were derived using the program DENZO.[20] No absorption correction was performed because of the rather regular crystal shape and small dimension of the specimen investigated. The structure was solved by direct methods (SHELXS-97) and refined with the SHELXL-97 program.[21,22]

Room-temperature X-ray powder diffraction data were collected employing a Guinier−Huber image plate system with monochromatic $CuK_{\alpha1}$ radiation ($8° < 2\theta < 100°$). Alternatively, a Siemens D500 diffractometer ($CoK_{\alpha1}$ radiation, step 0.01°, $18.5° \le 2\theta \le 92°$) was

dx.doi.org/10.1021/cm201584f |Chem. Mater. 2011, 23, 4016–4024

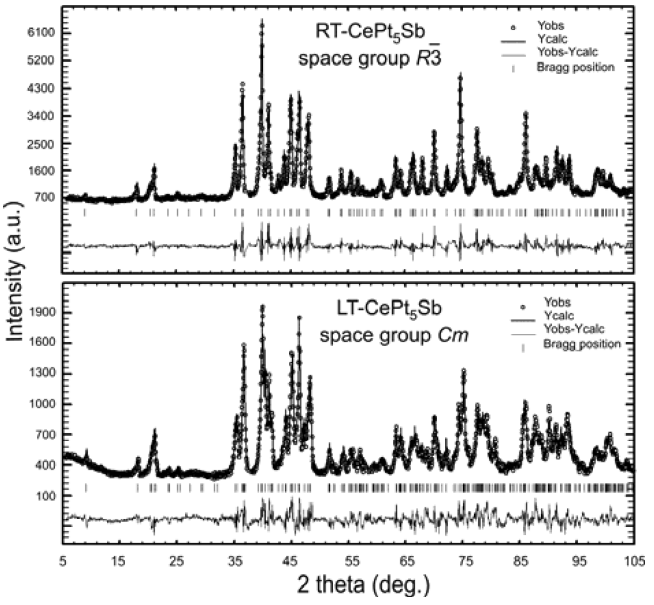

Figure 1. Neutron diffraction patterns of $CePt_5Sb$ collected at room temperature (upper panel) and at 4.2 K (lower panel). The solid line derives from the Rietveld refinement. $Y_{obsd} - Y_{calcd}$ is the intensity difference between experimental data and Rietveld calculations.

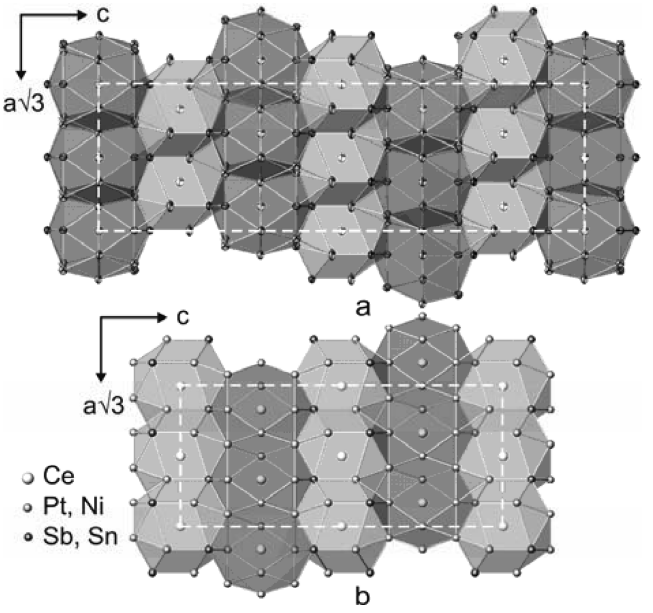

Figure 2. (a) RT-$CePt_5Sb$ unit cell in terms of spheres formed around Ce2 and Ce1 (in turn from left) in comparison with (b) $CeNi_5Sn$ structure. The orthohexagonal unit cells are outlined.

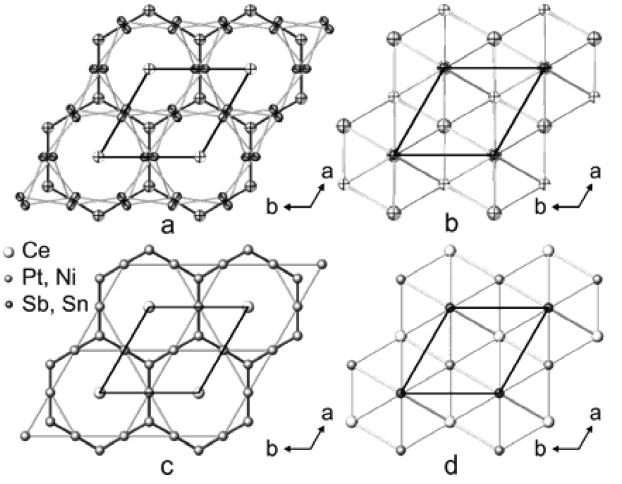

Figure 3. $CePt_5Sb$ structure represented as (a) $CaCu_5$-type and (b) $MnCu_2Al$-type derivative slabs vs $CeNi_5Sn$ structure (slabs of (c) $CaCu_5$-type and (d) $MnCu_2Al$-type). The unit cell of $CeNi_5Sn$ is displaced for 1/3, 2/3, 0. (a,c) 6^3 nets formed by Pt (Ni) atoms are drawn with black sticks; 3636 nets of transition metal atoms are shown with gray sticks. Ce−Pt (Ni) bonds are omitted. (b, d) Four-membered puckered nets of Ce and Pt (Ni) bonded to Sb (Sn) to form octahedra are drawn with gray sticks. For $CePt_5Sb$, the atoms are represented by their thermal ellipsoids.

used for recording room- and low-temperature (4.2 K) X-ray powder spectra. Neutron powder diffraction patterns were collected from a 5 g sample using the Echidna diffractometer at the OPAL reactor operated by the Australian Nuclear Science and Technology Organisation (ANSTO), Lucas Heights, Australia. The room temperature spectrum was collected over the range 4−164° (2θ), with a step size of 0.05°, using a wavelength of 1.622 Å. The sample powder was held in a 9 mm vanadium can and a 10′ collimator was used to improve the resolution at low 2θ. For the low-temperature measurements, the data were collected at 4.2 K by cooling the sample inside a top loading AS Scientific cryofurnace. Quantitative Rietveld refinements of both X-ray and neutron powder diffraction data were performed with the program FULLPROF.[23]

Physical Properties Measurements. A superconducting quantum interference device (SQUID) served for the determination of the magnetization from 2 K up to 300 K in fields up to 6 T. Pieces from the bulk specimens (~0.05 g) were used. The temperature dependent electrical resistivity was measured using a standard four-probe method on a bar cut from a polycrystalline sample (dimensions approximately 1 × 1 × 4 mm) in the temperature range 0.3−273 K using He3 setup (0.3−100 K) and a conventional setup (4.2−273 K). Heating and cooling were done at rates of less than 0.5 K/min, and resistance values were recorded in a drifting mode. The magnetic field-dependent resistivity at low temperatures was measured between 0 and 12 T. Specific heat measurements on samples of about 1 g were performed at temperatures ranging from 2 K up to 120 K by means of an adiabatic step heating technique.

RESULTS AND DISCUSSION

Structure Determination of $CePt_5Sb$ at Room Temperature. Single-crystal X-ray intensities with systematic extinctions for an *R*-centered Bravais lattice were compatible with the space groups $R3\overline{m}$, R3*m*, R32, $R\overline{3}$, and R3. Intensity statistics on $|E^2-1| = 0.7781$ favored a centrosymmetric space group.[24] Structure solution and refinement was performed for the two centrosymmetric space groups, $R3\overline{m}$ and $R\overline{3}$. Structure solution in $R3\overline{m}$ revealed 6 sites, which were assigned to 2 cerium (3*a* and 3*b*), 3 platinum (18*h*, 6*c*, and 6*c*) and 1 antimony (6*c*) atoms, in good correspondence with the nominal alloy composition. Further structure refinement ended at an unacceptably high reliability factor $R_F^2 - 0.20$. Moreover the isotropic thermal parameter for Pt1 located in the Wyckoff site 18*h* with .*m* point symmetry; *x*, $\overline{x}$, *z*, showed a U_{iso} value of about 4 times higher than for the other atoms, suggesting a removal of the mirror plane. Accordingly, the structure was successfully refined in the space group $R\overline{3}$ by

Table 2. Interatomic Distances in RT- and LT-$CePt_5Sb$

RT-$CePt_5Sb$

Ce1 − 6 Pt2 0.31526(2)	Pt1 − 2 Pt1 0.27018(5)	Pt1 − Ce2 0.37160(3)	Pt3 − 3 Ce2 0.30909(1)
Ce1 − 6 Pt1 0.32936(3)	Pt1 − 2 Pt1 0.27257(5)	Pt2 − Sb1 0.2520(1)	Pt3 − 3 Pt3 0.30911(1)
Ce1 − 6 Sb1 0.36278(5)	Pt1 − Pt3 0.27444(5)	Pt2 − 3 Pt1 0.27702(5)	Sb1 − Pt2 0.2520(1)
Ce2 − 6 Pt3 0.30909(1)	Pt1−- Pt2 0.27702(5)	Pt2 − 3 Ce1 0.31526(2)	Sb1 − 3 Pt1 0.26179(5)
Ce2 − 2 Sb1 0.32809(9)	Pt1 − Pt3 0.27876(5)	Pt2 − 3 Pt2 0.33310(3)	Sb1 − 3 Pt1 0.31007(4)
Ce2 − 6 Pt1 0.33238(3)	Pt1 − Sb1 0.31007(4)	Pt2 − 3 Sb1 0.33448(3)	Sb1 − Ce2 0.32809(9)
Ce2 − 6 Pt1 0.37159(5)	Pt1 − Ce1 0.32936(3)	Pt3 − 3 Pt1 0.27444(5)	Sb1 − 3 Pt2 0.33448(3)
Pt1 − Sb1 0.26179(5)	Pt1 − Ce2 0.33238(3)	Pt3 − 3 Pt1 0.27876(5)	Sb1 − 3 Ce1 0.36278(5)

LT-$CePt_5Sb$

Ce1 − Pt3 0.2903(2)	Pt1 − Pt1 0.2729(6)	Pt4 − Pt7 0.2684(6)	Pt7 − Ce2 0.2957(5)
Ce1 − 2 Pt5 0.3054(3)	Pt1 − Pt5 0.2833(8)	Pt4 − 2 Pt2 0.2740(2)	Pt7 − 2 Ce2 0.3144(5)
Ce1 − 2 Pt6 0.3096(8)	Pt1 − Pt3 0.2935(7)	Pt4 - Pt6 0.2756(4)	Pt7 − 2 Pt8 0.3181(9)
Ce1 − Pt6 0.3158(7	Pt1 − Sb1 0.2939(8)	Pt4 − 2 Sb2 0.2906(9)	Pt8 − Pt4 0.2643(1)
Ce1 − Pt4 0.3231(9)	Pt1 − Ce2 0.3230(5)	Pt4 − Ce1 0.3231(9)	Pt8 − 2 Pt1 0.2670(1)
Ce1 − 2 Pt2 0.3264(3)	Pt1 − Ce1 0.3513(2)	Pt4 − 2 Ce2 0.3487(1)	Pt8 − 2 Pt2 0.2773(1)
Ce1 − Pt5 0.3382(2)	Pt1 − Ce2 0.3655(8)	Pt5 − Sb2 0.2383(4)	Pt8 − Pt7 0.2890(1)
Ce1 − Sb2 0.3440(5)	Pt2 − Pt2 0.2104(9)	Pt5 − Pt3 0.2820(7)	Pt8 − 2 Ce2 0.2962(3)
Ce1 − 2 Pt1 0.3513(2)	Pt2 − Sb2 0.2538(5)	Pt5 − 2 Pt1 0.2833(8)	Pt8 − 2 Pt7 0.3181(9)
Ce1 − 2 Sb2 0.3541(7)	Pt2 − Pt4 0.2628(5)	Pt5 − Pt6 0.2989(1)	Pt8 − Pt3 0.3304(5)
Ce1 − Sb1 0.3639(1)	Pt2 − Pt4 0.2740(2)	Pt5 − 2 Ce1 0.3054(3)	Pt8 − Ce2 0.3339(5)
Ce1 − 2 Sb1 0.3844(9)	Pt2 − Pt6 0.2748(2)	Pt5 − Sb1 0.3319(7)	Sb1 − Pt6 0.2666(4)
Ce2 − Pt7 0.2957(5)	Pt2 − Pt8 0.2773(1)	Pt5 − Ce1 0.3382(2)	Sb1 − 2 Pt1 0.2717(6)
Ce2 − 2 Pt8 0.2962(3)	Pt2 − Pt7 0.2774(5)	Pt5 − 2 Pt6 0.3454(5)	Sb1 − 2 Pt3 0.2752(4)
Ce2 − 2 Pt2 0.3045(6)	Pt2 − Ce2 0.3045(6)	Pt5 − 2 Sb1 0.3477(3)	Sb1 − 2 Pt1 0.2939(8)
Ce2 − Sb1 0.3129(7)	Pt2 − Sb2 0.3241(1)	Pt6 − Sb1 0.2666(4)	Sb1 − Ce2 0.3129(7)
Ce2 − 2 Pt7 0.3144(5)	Pt2 − Pt2 0.3261(1)	Pt6 − 2 Pt2 0.2748(2)	Sb1 − Pt5 0.3319(7)
Ce2 − 2 Pt1 0.3230(5)	Pt2 − Ce1 0.3264(3)	Pt6 − Pt4 0.2756(4)	Sb1 − 2 Pt5 0.3477(3)
Ce2 − Sb2 0.3337(7)	Pt2 − Ce2 0.3907(5)	Pt6 − Pt5 0.2989(1)	Sb1 − Ce1 0.3639(1)
Ce2 − Pt8 0.3339(5)	Pt3 − 2 Pt1 0.2494(4)	Pt6 − 2 Ce1 0.3096(8)	Sb1 − 2 Ce1 0.3844(9)
Ce2 − 2 Pt4 0.3487(1)	Pt3 − 2 Sb1 0.2752(4)	Pt6 − Ce1 0.3158(7)	Sb2 − Pt5 0.2383(4
Ce2 − 2 Pt1 0.3655(8)	Pt3 − Pt7 0.2803(3)	Pt6 − Sb2 0.3281(8)	Sb2 − 2 Pt2 0.2538(5
Ce2 − 2 Pt3 0.3852(1)	Pt3 − Pt5 0.2820(7)	Pt6 − 2 Sb2 0.3317(6)	Sb2 − 2 Pt4 0.2906(9
Ce2 − 2 Pt2 0.3907(5)	Pt3 - Ce1 0.2903(2)	Pt6 − 2 Pt5 0.3454(5)	Sb2 − 2 Pt2 0.3241(1
Pt1 − Pt3 0.2494(4)	Pt3 − 2 Pt1 0.2935(7)	Pt7 − 2 Pt1 0.2682(5)	Sb2 − Pt6 0.3281(8
Pt1 − Pt1 0.2639(4)	Pt3 − Pt8 0.3304(5)	Pt7 − Pt4 0.2684(6)	Sb2 − 2 Pt6 0.3317(6)
Pt1 − Pt8 0.2670(1)	Pt3 − 2 Ce2 0.3852(1)	Pt7 − 2 Pt2 0.2774(5)	Sb2 − Ce2 0.3337(7
Pt1 − Pt7 0.2682(5)	Pt4 − 2 Pt2 0.2628(5)	Pt7 − Pt3 0.2803(3)	Sb2 − Ce1 0.3440(5
Pt1 − Sb1 0.2717(6)	Pt4 − Pt8 0.2643(1)	Pt7 − Pt8 0.2890(1)	Sb2 − 2 Ce1 0.3541(7

full-matrix least-squares methods on F^2 with satisfactory values of anisotropic displacement parameters for all atoms. The refinement, which converged to $R_F{}^2 = 0.024$ with residual electron densities smaller than ±3530 electrons/nm^3, revealed a new type of atom arrangement (see Table 1). Trial refinements in the space groups *R*3*m*, *R*32, and *R*3 did not lead to satisfactory results. The atomic coordinates obtained from the single-crystal study, were used in the starting model for the Rietveld analyses of X-ray and neutron powder diffraction data collected at room temperature. The refinements converged to low residual values ($R_F = \Sigma|F_o - F_c|/\Sigma F_o = 0.034$, $R_I = \Sigma|I - I_c|/\Sigma I_o = 0.062$ for X-ray and $R_F = \Sigma|F_o - F_c|/\Sigma F_o = 0.048$, $R_I = \Sigma|I_o - I_c|/\Sigma I_o = 0.074$ for neutron data) confirming the structure model derived from the single crystal. A Rietveld refinement of neutron diffraction data at room temperature is shown in the upper panel of Figure 1.

Structure Determination of $CePt_5Sb$ at Low Temperature from X-ray and Neutron Powder Diffraction. Examination of the low -temperature X-ray and neutron diffraction patterns revealed the presence of a number of peaks inconsistent with the rhombohedral unit-cell observed from X-ray single crystal and powder diffraction studies at room temperature implying a structural transition. Although diffraction peaks within the 1 nm ≤ *d* ≤ 0.2 nm range of the neutron diffraction spectrum could be well indexed (TREOR90[26]) by orthohexagonal unit cells related to the RT-$CePt_5Sb$ metric, the profile fitting procedure (WINPLOTR[23]) revealed the absence of prominent splitting of certain reflections. A significant improvement was achieved when the pattern was fitted with a monoclinic unit cell $a = 0.9182$ nm, $b = 0.5369$ nm, $c = 1.0806$ nm, $\beta = 107.40°$. The extinctions in the new pattern indicated three possible space groups: *C*2, *Cm* and *C*2/*m*. Applying the program EXPO[27,28] in combination with the

dx.doi.org/10.1021/cm201584f |*Chem. Mater.* 2011, 23, 4016–4024

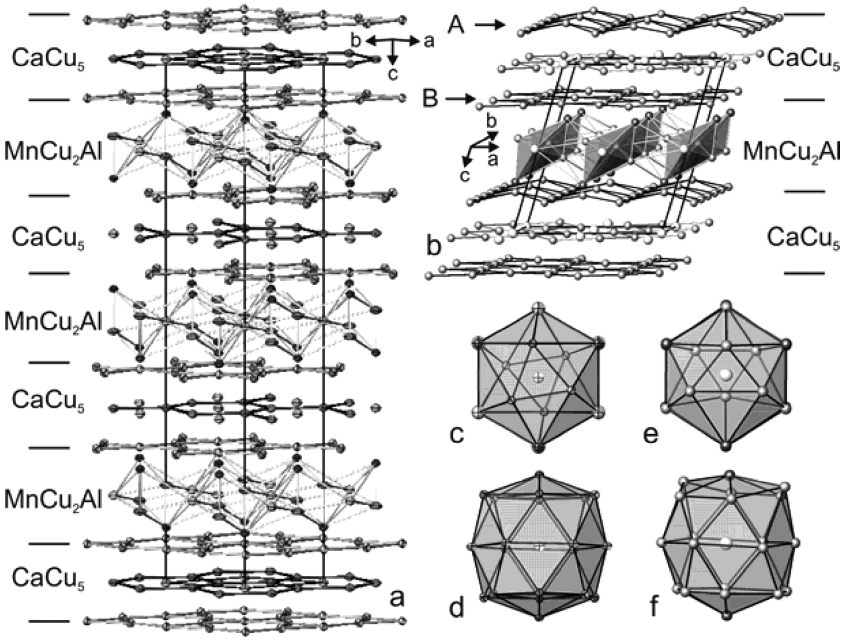

Figure 4. (a) RT- and (b) LT- $CePt_5Sb$ structures. Consecutive $CaCu_5$- and $MnCu_2Al$-type blocks are indicated. Bonds between layers and blocks are omitted for clarity. The origin of LT-structure is shifted into Ce2 position at 0.526, 0, 0.261. The empty octahedra in $MnCu_2Al$-type fragment are outlined. Corrugated and flat platinum nets are denoted as A and B respectively. Atom environment of Ce1 and Ce2 in the (c, d) RT-$CePt_5Sb$ and (e, f) LT-$CePt_5Sb$.

knowledge of the RT-phase structural features it was possible to build a reasonable structural model. Among the three possible space groups, *Cm* was chosen as the best suited because it led to a stable Rietveld refinement (Figure 1) yielding realistic values for anisotropic displacement factors, occupancy parameters, and interatomic distances (Table 1, 2).

Structure Description and Relationships. The RT-$CePt_5Sb$ structure (space group $R\bar{3}$, a = 0.53535(2) nm, c = 3.10814-(12) nm) is related to $CeNi_5Sn$ (space group $P6_3/mmc$, a = 0.49049 nm, c = 1.9731 nm), which was reported to consist of $CaCu_5$-blocks and fragments of the Heusler structure $MnCu_2Al$ alternating along the z-direction.[17,29] Similarly to $CeNi_5Sn$, the structure of RT-$CePt_5Sb$ is composed of sheets built of face-connected 18- and 20-edged coordination polyhedra of Ce1 (Heusler-phase fragment) and Ce2 ($CaCu_5$-type block) atoms; those sheets extend infinitely parallel to the *ab* plane (Figure 2). The closest environment of Pt2 is a distorted cube with one edge replaced by three Pt1 atoms; three more Pt2 atoms, located against the faces of a cube at the distance 0.3331 nm from the central atom complete its coordination sphere (Table 2). Sb is surrounded by 14 atoms including three Ce1 atoms at a rather long distance of 0.36278 nm. While Heusler phase fragments are rather similar in both structures, the $CaCu_5$-block in RT-$CePt_5Sb$ is significantly deformed as compared to the corresponding block in $CeNi_5Sn$ (Figure 3). The closest coordination environment for Pt3 is formed by six Pt1 exhibiting the distorted trigonal-prismatic orientation of bond directions; similarly to other $CaCu_5$-type related structures, three Ce2 (located at the distance 0.30909 nm) and three Pt3 atoms (at 0.30911 nm) are included in the coordination sphere of Pt3 (Table 2). Pt1 is coordinated by 12 atoms forming a distorted icosahedron.

$CaCu_5$- and $MnCu_2Al$-fragments are also preserved in the monoclinic LT-$CePt_5Sb$ structure, although with a higher degree of deformation. In the Heusler-type unit, the rhombohedral-to-monoclinic transition mainly involves the distortion of Pt−Sb bonds, connecting Pt5 and Sb2 atoms at the close contact distance of 0.2383 nm thus producing asymmetric shrinkage of empty octahedra [$Ce_2Pt_2Sb_2$] with the center at 0,0,1/2 (the polyhedra are highlighted in Figure 4b). The reason is that in the RT-structure the antimony atom resides in one Wyckoff site 6*c* (0,0,*z*; z = 0.33402(2)) while in LT-$CePt_5Sb$ this site is split in two 2*a* sites (x,0,z; x = 0.439(3); z = 0.958(3) and x = 0.663(3); z = 0.584(3)) which both are slightly displaced from the antimony atom position in the RT-structure. This displacement affects the coordination sphere also of Ce1 consequently leading to an elongated distance Ce1−Sb1 of 0.3844 nm. The coordination of Ce2 in the LT-$CePt_5Sb$ is influenced by structural changes, which occur within the $CaCu_5$-block. Originally, in the RT $R\bar{3}$ structure the $CaCu_5$ fragment is composed of two distorted flat 3636 kagomé nets formed by symmetry-equivalent Pt1 atoms and by the flat 6^3 net of Pt3 which is located between two 3636 nets and accommodates Ce atoms (two outer layers and inner layer respectively in the $CaCu_5$ block in Figure 4a). In LT-$CePt_5Sb$, the flat shape is maintained for the nets formed by Pt2 and Pt4 (denoted as B in Figure 4b), whereas the nets formed by Pt1 and Pt3 atoms (A in Figure 4b) are corrugated because of rearrangement of the constituent atoms. Such reconstruction of Pt nets brings the Pt3 atoms rather close to Ce1 (0.2903 nm). The coordination polyhedra of Ce1 and Ce2 for both RT- and LT-structure are shown in Figure 4c−f for comparison. The rearrangement of Pt atoms also affects the shape of the nearest trigonal-prismatic atom environment of Pt7 and Pt8 in the LT structure. In RT-$CePt_5Sb$, Pt3 is surrounded by six platinum atoms which constitute two 3636 kagomé nets with the bond distances $d_{Pt3-Pt1}$ of 0.27444 and 0.27876 nm (Table 2, Figure 5a). As a consequence of the rhombohedral-to-monoclinic distortion in LT-$CePt_5Sb$, the nearest atom environments of Pt7 and Pt8 are formed by four atoms (Pt1, Pt2, Pt3 and Pt4)

dx.doi.org/10.1021/cm201584f |*Chem. Mater.* 2011, 23, 4016–4024

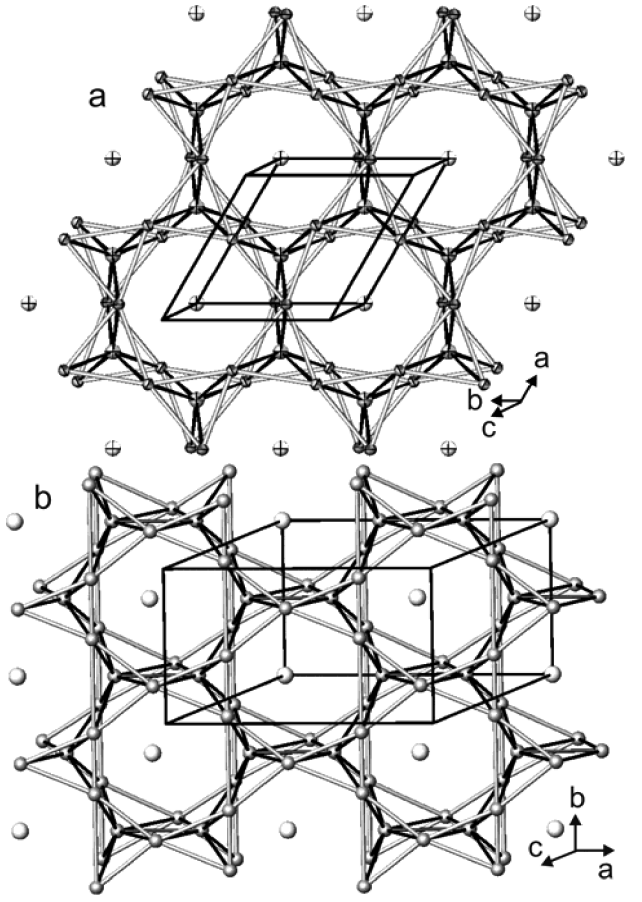

Figure 5. Distorted 3636 Kagomé nets of platinum atoms in RT-$CePt_5Sb$ (slab at z within −0.075 to 0.075) in comparison with those in LT-$CePt_5Sb$ (slab at z within 0−0.5) (a and b, respectively) (light gray sticks). The nearest (a) [Pt_6] coordination of Pt3 and (b) [Pt_7] coordination of Pt7 and Pt8 are emphasized with black sticks. The origin of the LT-structure is shifted to 0.526, 0, 0.261.

located in two 4*b* and two 2*a* Wyckoff sites, respectively. Because of the spatial movement of Pt3 rather far along the *c*-axis toward the $MgCu_2Al$-type block, the atom Pt7 becomes located closer to the central Pt8 ($d_{Pt7-Pt8}$ = 0.2890 nm) thus completing its nearest coordination sphere (Figure 5b). Concomitantly, the coordination sphere of Ce2 is also enlarged exhibiting elongated distances to the neighboring Pt2 and Pt3 atoms (0.3852 and 0.3907 nm, respectively) as compared to the RT-structure (Ce2−Pt1 0.3717 nm). The restructuring of part of the 3636 nets and accordingly, the displacement of the Pt3 atom leads to the loss of the center of symmetry; consequently, the LT structure can not be described within the centrosymmetric space group *C*2/*m*.

The space groups of the two structural modifications of $CePt_5Sb$, $R\bar{3}$ and *Cm*, do not have a group-subgroup relationship; the phase transformation is therefore first order. The unit cells of RT-$CePt_5Sb$ (*a*, *b*, *c* in orthohexagonal setting) and LT-$CePt_5Sb$ (a', b', c', β') are geometrically related via a simple transformation matrix $a' = -b$, $b' = -a$, $c' = {}^1/_3b - {}^1/_3c$ (Figure 6).

Magnetism. Results of magnetic measurements are presented in Figure 7 as the temperature-dependent inverse magnetic susceptibility at 0.5 T. The compound $CePt_5Sb$ behaves paramagnetic in the temperature region studied and no magnetic transition is observed. Despite this, around 80 K a slight change

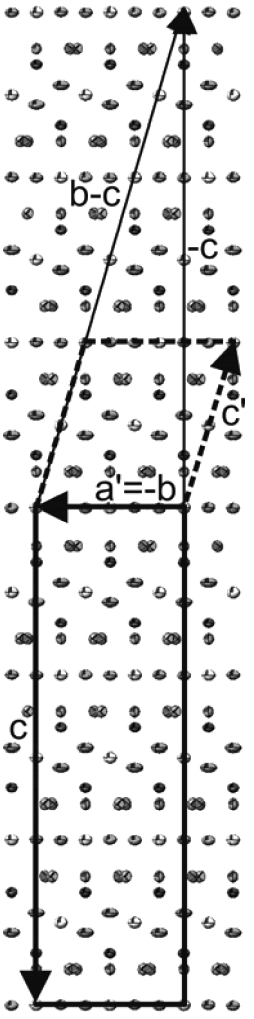

Figure 6. Geometrically deduced relationships between RT-$CePt_5Sb$ (orthohexagonal setting, solid lines) and LT-$CePt_5Sb$ (origin shifted to 0.526, 0, 0.261, dashed lines) unit cells. *a*, *b*, *c* and a', b', c' denote the vectors of the RT- and LT-$CePt_5Sb$ unit cells, respectively.

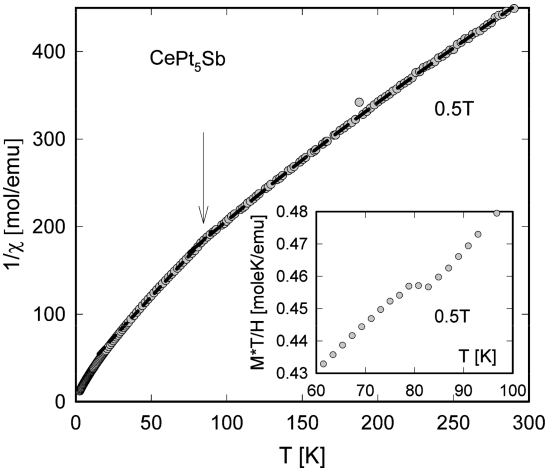

Figure 7. Temperature-dependent inverse magnetic susceptibility of $CePt_5Sb$. An arrow is pointing to a small kink at the transition temperature. The inset shows the 0.5 T M^*T/H curve of $CePt_5Sb$.

dx.doi.org/10.1021/cm201584f |*Chem. Mater.* 2011, 23, 4016–4024

in the slope of the curve $\chi^{-1}(T)$ is recognized. This anomaly becomes more pronounced when plotted as M^*T/H. The change of the slope of $\chi^{-1}(T)$ at 80 K results in different magnetic properties for $T > 80$ K and $T < 80$ K. Fits according to a modified Curie−Weiss law were performed for the high-temperature (above 80 K) and low -temperature (20−80 K) range yielding $\mu^{HT} = 2.18\ \mu_B$, $\theta_P{}^{HT} = -33$ K and $\mu^{LT} = 2.07\ \mu_B$, $\theta_P{}^{LT} = -14$ K, respectively. In both states, the effective magnetic moment of Ce is smaller compared to the one expected for Ce^{3+} (2.54 μ_B). Crystalline electric field effects that lift the 6-fold degenerated ground state of Ce^{3+} reduces, in general, the effective magnetic moment below 2.54 μ_B. At sufficiently high temperature, however, the free ion value is recovered. Minor modifications might be attributed to the Kondo effect, as well. The negative paramagnetic Curie temperatures point to the dominant role of antiferromagnetic and/or Kondo interactions in both states. In accordance with the structural change observed from the neutron and X-ray data, the anomaly in M^*T/H observed around 80 K might be associated with the structural phase transition from $R\bar{3}$ to Cm. Different structural types give rise to different crystal field effects, and consequently magnetic properties may differ at high and low temperatures.

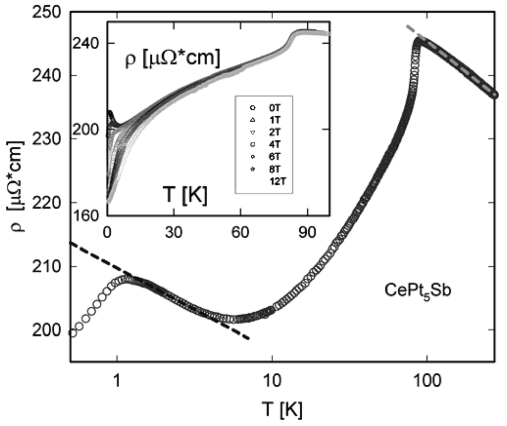

Figure 8. Resistivity curve of $CePt_5Sb$ measured in zero-magnetic field in a semilogarithmic plot. The inset shows the influence of the magnetic field on the resistivity. Dashed lines are fits according to text.

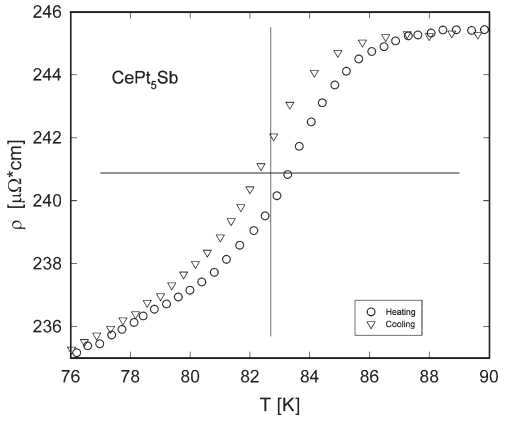

Figure 9. Resistivity hysteresis of $CePt_5Sb$ in zero magnetic field. Transition temperature determined to be 83 K by the procedure described in text.

Electrical Resistivity. Results of zero-field measurements are presented in Figure 8. With the decrease in temperature the resistivity of the sample rises weakly down to around 85 K where a sharp drop of $\rho(T)$ is observed. Such a change of the resistivity is, in general, attributed to a first-order phase transition. With temperatures further decreasing, the material behaves metallic and the resistivity drops until 5.6 K where again an increase is observed with a maximum around 1 K. With application of a magnetic field, the resistivity of $CePt_5Sb$ decreases in the whole temperature range studied (see inset Figure 8) pointing to the dominant influence of disordered magnetic moments. The maximum in the low temperature region shifts to higher temperatures and eventually becomes suppressed for fields around 2 T.

At low temperatures, below about 10 K, $\rho(T)$ is typical for compounds exhibiting the Kondo effect in presence of a strong crystalline electric field influence. The logarithmic temperature dependence of the curve as well as the behavior in magnetic fields support such an assumption. The drop of $\rho(T)$ below 1 K is reminiscent for the onset of long-range magnetic order.

In the high-temperature region, the compound seems to exhibit characteristic features of an insulator (high absolute value and positive temperature derivative of resistivity). However, for $CePt_5Sb$, this behavior is more likely of a magnetic origin. As a result of a least-squares fit, the slope of the resistivity at high temperatures was found to be logarithmical and can be described by $\rho(T) = (\rho_0 + \rho_\infty) + bT + c_k \ln T$, a formula common for the resistivity of Kondo lattices.

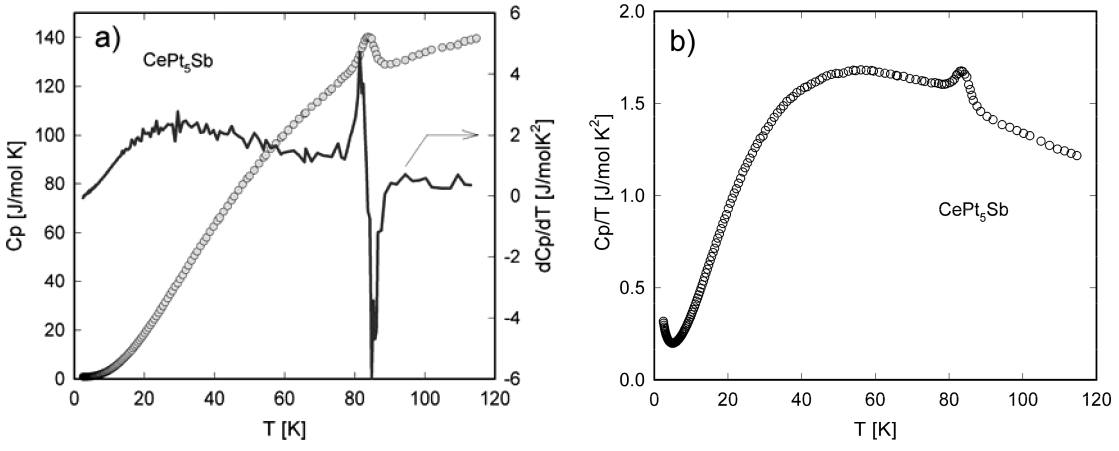

Figure 10. (a) Temperature-dependent specific heat of $CePt_5Sb$. The derivative dC_p/dT hints the transition to be of the first order. (b) Specific heat C_p/T vs T of $CePt_5Sb$.

dx.doi.org/10.1021/cm201584f |Chem. Mater. 2011, 23, 4016–4024

Figure 9 exhibits the resistivity data of $CePt_5Sb$ collected on cooling and heating of the sample in the vicinity of the transition. A small but prominent hysteresis is observed as expected for a first order phase transition. To determine the exact temperature of the transition T_{TRANS}, the balance between $\int_{T_L}^{T_{TRANS}}(\rho_H(T) - \rho_C(T))dT$ and $\int_{T_{TRANS}}^{T_H}(\rho_H(T) - \rho_C(T))dT$, needs to be achieved, where $\rho_H(T)$, $\rho_C(T)$ are heating and cooling resistivity values; T_H and T_L are high and low temperatures where the difference between both curves becomes negligible (75 and 90 K in our case). As a result of a least-squares fit, T_{TRANS} = 83 K was derived.

Specific Heat. The specific heat data $C_P(T)$ of $CePt_5Sb$ are shown in Figure 10a. The distinct anomaly at 83 K is attributed to the phase transition already recalled from the resistivity and susceptibility data. Although the increase in specific heat at the transition temperature is far from infinity, the behavior of the derivative indicates the transition to be of first order. Rather small differences in the absolute values of specific heat below and above the transition temperature are due to insignificant changes in the vibrational structure of the lattice, supporting the close relationship between the high- and low-temperature structures. The low-temperature increase in C_p/T vs T (Figure 10b) seen below 5 K is expected to be caused by the Kondo effect. Theoretically, and in the case of a doublet as ground state, a maximum value of 1.5 J/(mol K) is reached at $T \approx 0.67\ T_K$.[30] Magnetic order, however, modifies such a universal behavior, and entropy released at the phase transition is spread toward higher temperatures. On further cooling below 1 K, the magnetic phase transition, concluded from resistivity data, would manifest itself by a λ-like anomaly, reduced in height due to acting of the Kondo effect.

CONCLUSIONS

The new antimonide $CePt_5Sb$ crystallizes with a unique type of structure (space group $R\bar{3}$, $a = 0.53535(2)$ nm, $c = 3.10814(12)$ nm). The structure comprises $CaCu_5$- and $MnCu_2Al$- fragments alternating along the z-axis. On cooling, RT-$CePt_5Sb$ undergoes a structural transformation at about 80 K. The monoclinic unit cell can be geometrically deduced from the orthohexagonal one via the transformation matrix $a' = -b$, $b' = -a$, $c' = {}^1/_3b - {}^1/_3c$. The structural distortion due to the orthohexagonal-to-monoclinic transition is rather small (the decrease in volume is ~1.2%) leading to slight deviations in lattice parameters a, b, and c and to a more pronounced alteration of the monoclinic angle β: a = 0.91821(5) nm, b = 0.53696(1) nm, c = 1.08064(6) nm, β = 107.40(1)°. However, the distortions on the atomic level in the unit cell are more significant causing the corrugation of platinum layers and the modification of atomic coordination spheres. The low-temperature structural transition was elaborated from magnetic, specific heat, and resistivity measurements, confirming its first-order character. The physical behavior at low temperatures is governed by Kondo effect in presence of crystalline electric field effects. Below about 1 K, resistivity data refer to the onset of long-range magnetic order, developing in a doublet as crystalline electric field ground state.

ASSOCIATED CONTENT

Supporting Information. Crystallographic information file (CIF).This material is available free of charge via the Internet at http://pubs.acs.org.

AUTHOR INFORMATION

Corresponding Author

*E-mail: bauer@ifp.tuwien.ac.at.

Present Addresses

⊥MANA, NIMS, 1−1 Namiki, Tsukuba 305−0044, Japan

ACKNOWLEDGMENT

Research supported by Austrian National Science Foundation FWF projects M1067-N20. L.S. is grateful to the ÖAD for an Ernst Mach fellowship at the Vienna University of Technology.

REFERENCES

(1) Kauzlarich, S. M. *Chemistry, Structure and Bonding of Zintl Phases and Ions*; VCH Publishers: New York, 1996.

(2) Sato, H.; Sugawara, H; Aoki, Y.; Harima, H. In *Handbook of Magnetic Materials*; Buschow, K. H. J., Ed.; Elsevier B.V.: Amsterdam, 2009; Vol. 18, pp 1−110.

(3) Mills, A. M.; Lam, R.; Ferguson, M. J.; Deakin, L.; Mar., A. *Coord. Chem. Rev.* **2002**, *233−234*, 207–222.

(4) Sologub, O.; Salamakha, P. S. In *Handbook on the Physics and Chemistry of Rare Earths*; Gschneidner, K. A.; Bünzli, J.-C. G.; Pecharsky, V. K., Eds.; Elsevier: Amsterdam, 2003; Vol. 33, pp 35−146.

(5) Kleinke, H. *Chem. Mater.* **2010**, *22*, 604–611.

(6) Snyder, G. J.; Toberer, E. S. *Nat. Mater.* **2008**, *7*, 105–114.

(7) Kauzlarich, S. M.; Brown, S. R.; Snyder, G. J. *Dalton Trans.* **2007**, 2099–2107.

(8) Salzgeber, K.; Prenninger, P.; Grytsiv, A.; Rogl, P.; Bauer, E. *J. Electron. Mater.* **2010**, *39*, 2074–2078.

(9) Aeppli, G.; Fisk, Z. *Comments Condens. Matter. Phys.* **1992**, *16*, 155–165.

(10) Jones, C. D. W.; Regan, K. A.; DiSalvo, F. J. *Phys. Rev. B* **1998**, *58* (24), 16057–16063.

(11) Takabatake, T.; Tanaka, H.; Bando, Y.; Fujii, H.; Nishigori, S.; Suzuki, T.; Fujita, T.; Kido, G. *Phys. Rev. B* **1994**, *50*, 623–626.

(12) Sasakawa, T.; Shigetoh, K.; Hirata, D.; Umeo, K.; Takabatake, T. *Phys. B: Condens. Mater.* **2005**, *359−361*, 111–114.

(13) Gofryk, K.; Kaczorowski, D.; Plackowski, T.; Leithe-Jasper, A.; Grin, Yu. *Phys. Rev. B 72* **2005**, 094409−1–7.

(14) Sologub, O. L.; Salamakha, L. P.; Noël, H.; Roisnel, T.; Gonçalves, A. P. *J. Alloys Compd.* **2008**, *450*, 215–221.

(15) Parthé, E.; Chabot, B. In *Handbook on the Physics and Chemistry of Rare Earths*; Gschneidner, K. Jr., Eyring, L., Eds.; Elsevier: Amsterdam, 1984; Vol. 6, pp113−334.

(16) Rogl, P. In *Inorganic Reactions and Methods*; Zuckerman, J. J., Ed.; VCH-Publications Inc.: Weinheim, Germany, 1991; Vol. 13, pp 85−167.

(17) Skolozdra, R. V. In *Handbook on the Physics and Chemistry of Rare Earths*, Gschneidner, K. Jr., Eyring, L., Eds.; Elsevier: Amsterdam, 1997; Vol. 24, pp 399−516.

(18) Liu, Y.; Pan, H.; Gao, M.; Wang, Q. *J. Mater. Chem.* **2011**, *21*, 4743–4755.

(19) Strnat, K. J. In *Ferromagnetic Materials*, Wohlfarth, E. P., Buschow, K. H., Eds.; Elsevier: Amsterdam, 1988; Vol. 4, pp 131−209.

(20) *Nonius Kappa CCD, Program Package COLLECT, DENZO, SCALEPACK, SORTAV*; Nonius: Delft, The Netherlands.

(21) Sheldrick, G. M. *SHELXS-97, Program for the Solution of Crystal Structures*; University of Göttingen: Göttingen, Germany, 1997.

(22) Sheldrick, G. M. *SHELXS-97, Program for Crystal Structure Refinement*; University of Göttingen: Göttingen, Germany, 1997.

(23) Rodriguez-Carvajal, J. *Phys. B* **1993**, *192*, 55.Roisnel, T.; Rodriguez-Carvajal, J. In *Proceedings of the Materials Science Forum, European Powder Diffraction Conference (EPDIC 7)*; Trans Tech Publications: Zurich, Switzerland, 2000; p 118.

(24) Marsh, R. E. *Acta Crystallogr.* **1995**, *B51*, 897–907.

(25) Parthé, E.; Gelato, L.; Chabot, B.; Penzo, M.; Censual, K.; Gladyshevskii, R. *TYPIX — Standardized Data and Crystal Chemical Characterization of Inorganic Structure Types*; Springer-Verlag: Berlin, 1994.
(26) Werner, P.-E.; Eriksson, L.; Westdahl, M. *J. Appl. Crystallogr.* **1985**, *18*, 367–370.
(27) Altomare, A.; Burla, M. C.; Cascarano, G.; Giacovazzo, C.; Guagliardi, A.; Moliterni, A.; Polidori, G. *J. Appl. Crystallogr.* **1995**, *28*, 842–846.
(28) Altomare, A.; Cascarano, G.; Giacovazzo, C.; Guagliardi, A.; Burla, M. C.; Polidori, G.; Camalli, M. *J. Appl. Crystallogr.* **1994**, *27*, 435–436.
(29) Cenzual, K.; Parthé, E. *Acta Crystallogr., Sect. C* **1984**, *40*, 1127–1131.
(30) Oliveira, L. N.; Wilkins, J. W. *Phys. Rev. Lett.* **1981**, *47*, 1553–1556.